Dry mass photometry of single bacteria using quantitative wavefront microscopy

Maëlle Bénéfice, Aurore Gorlas, Baptiste Marthy, Violette da Cunha, Patrick Forterre, Anne Sentenac, Patrick C Chaumet, Guillaume Baffou

Dry mass photometry of single bacteria using quantitative wavefront microscopy

Maëlle Bénéfice,[1] Aurore Gorlas,[2] Baptiste Marthy, Violette Da Cunha,[2] Patrick Forterre,[2,3] Anne Sentenac,[1] Patrick C. Chaumet,[1] Guillaume Baffou[1,*]

[1] Institut Fresnel, CNRS, Aix Marseille University, Centrale Marseille, Marseille, France

[2] Université Paris-Saclay, CEA, CNRS, Institute for Integrative Biology of the Cell (I2BC), 91198, Gif-sur-Yvette, France

[3] Département de Microbiologie, Institut Pasteur, 75015 Paris, France

* email: guillaume.baffou@fresnel.fr

ABSTRACT

Quantitative phase microscopy (QPM) represents a non-invasive alternative to fluorescence microscopy for cell observation with high contrast and for the quantitative measurement of dry mass (DM) and growth rate at the single cell level. While DM measurements using QPM have been widely conducted on mammalian cells, bacteria have been less investigated, presumably due to the high-resolution and high-sensitivity required by their smaller size. This article demonstrates the use of cross-grating wavefront microscopy (CGM), a high-resolution and high-sensitivity QPM, for accurate DM measurement and monitoring of single micro-organisms (bacteria and archaea). The article covers strategies for overcoming light diffraction and sample focusing, and introduces the concepts of normalized optical volume (OV) and optical polarizability (OP) to gain additional information beyond DM. The algorithms for DM, OV, and OP measurements are illustrated through two case studies: monitoring dry mass evolution in a microscale colony forming unit as a function of temperature, and using OP as a potential species-specific signature.

SIGNIFICANCE

Quantitative phase microscopy techniques are capable of measuring the dry mass of biological cells in culture using optical microscopy means, usually for eukaryotic cells in the hundred picogram range. This study provides the guidelines for accurately measuring dry masses in the sub-picogram range, for the study of micro-organisms, such as bacteria or archaea, opening the path for the precise monitoring of bacteria growth at the single cell level. Moreover, this study extends the possibilities of quantitative phase microscopies by introducing new measurables quantities besides dry mass, such as the complex

optical polarisability and the normalized optical volume, with envisioned applications in cell classification using deep learning.

INTRODUCTION

Mass density and refractive index of transparent materials are closely related. This trend is far from being a universal law for *organic* and *inorganic* materials, as stressed in 1954 by Barr, who objectively compared a wide range of materials[1]. For *biological* matter, however, it is widely recognized that an increase in mass density results in a corresponding increase in the refractive index, especially when the system of interest is mainly composed of proteins.[2–4] The law holds true for living cells for instance, where the mass density ρ and the refractive index n of the cell are linked by the relation

$$n - n_{\text{water}} = \gamma(\rho - \rho_{\text{water}}), \tag{1}$$

where γ, called the specific refraction increment, is roughly constant, varying within the tight range 0.18 to 0.21 μm^3·pg^{-1} (we chose $\gamma = 0.20$ μm^3·pg^{-1} in this manuscript). ρ_{water} and n_{water} are the mass density and refractive index of water. Water is taken as the reference liquid because cells are normally living and cultured in aqueous environment.

Based on this relation, Barer initiated in 1954 the idea of using phase imaging to measure the dry mass of cells.[2] Indeed, quantitative phase microscopy (QPM) techniques map the phase shift ϕ, or equivalently the optical path difference (OPD) $\delta\ell = \phi\lambda/2\pi$, associated with a transparent object of interest in the field of view of a microscope, typically biological media like living cells. The measured OPD image reads

$$\delta\ell(x,y) = \int (n(x,y,z) - n_{\text{water}})\mathrm{d}z. \tag{2}$$

The integral runs over the thickness of the imaged object. The so-called optical volume (OV) δV is defined as the integral of the OPD over the area of interest

$$\delta V = \iint \delta\ell(x,y)\mathrm{d}x\mathrm{d}y = \iiint (n(x,y,z) - n_{\text{water}})\mathrm{d}x\mathrm{d}y\mathrm{d}z \tag{3}$$

and can be simply retrieved from OPD images by a pixel summation. From Eqs. (1) and (3), one can derive the important equation linking the measured OPD ($\delta\ell$) or phase (ϕ) image with the dry mass (DM) δm of the imaged object:

$$\delta m = \gamma^{-1} \iint \delta\ell(x,y)\mathrm{d}x\mathrm{d}y, \tag{4}$$

$$\delta m = \gamma^{-1} \frac{\lambda}{2\pi} \iint \phi(x,y)\mathrm{d}x\mathrm{d}y. \tag{5}$$

The dry mass is considered as a faithful estimation of the biomass of the system, more than the fresh mass that does not exclude water, and especially in cell biology. Imaging also enables the mapping of the dry mass surface density (DMSD) $\delta\sigma$, in pg·μm^{-2}:

$$\delta\sigma(x,y) = \gamma^{-1}\delta\ell(x,y). \quad (6)$$

This relation directly leads to the simple relation between OV and DM:

$$\delta m = \gamma^{-1}\delta V.$$

Here are the relations to be used in practice, including the common units:

$$\delta\sigma(x,y)\ [\mathrm{pg/\mu m^2}] = 5.0 \times 10^{-3}\ \delta\ell(x,y)\ [\mathrm{nm}].$$

$$\delta m\ [\mathrm{pg}] = 5.0\ \delta V\ [\mathrm{\mu m^3}].$$

Although the idea of measuring biomass using QPM was introduced in 1954, its implementation remained elusive for 50 years.[5,6] One had to wait for the development of high-resolution QPM techniques in the 2000s to observe the publication of the first influential articles on this topic. In 2008, Popescu *et al.* illustrated the principle of dry mass measurement of living cells using QPM in a seminal article by measuring the dry mass of HeLa cells.[7] The authors could measure cell biomasses of a few hundred pg using two QPM techniques, namely Fourier phase microscopy (FPM) and Hilbert phase microscopy (HPM). The group reported a sensitivity of 4 fg·μm^{-2}. Simultaneouly, the Marquet's group reported measurements of the dry mass production rate of yeast cells using digitial holography microscopy (DHM).[8] Dry masses of wild-type and mutant cells of a few 10s of pg were measured and followed through the cell cycle. In 2011, another seminal article was published by the group of Popescu using, this time, spatial light interference microscopy (SLIM) and focusing on *Escherichia coli (E. coli)*.[9] Dry masses of a few pg were measured, demonstrating the ability of QPM to answer the important question whether cell growth is linear or exponential. In 2012, Girshovitz and Shaked introduced the wide variety of mass-OPD-related physical quantities that can be measured by QPM, besides dry mass and DMSD, namely the optical volume, the cell outer surface, some phase/mass ratiometric quantities, sphericity/eccentricity indices and some statistical parameters (phase kurtosis and skewness)[10]. The interest of all these quantities was illustrated by using HeLa cells.

Quadriwave lateral shearing interferometry (QLSI) is a high-resolution optical wavefront imaging technique. QLSI is simply based on the use of a 2-dimentional (2D) diffraction grating (aka cross-grating) placed at a millimetric distance from the sensor of a camera.[11] When a QLSI camera is implemented on a microscope, it can then be refered to as cross-grating wavefront microscopy (CGM).[12,13] In 2015, Aknoun et al. introduced the use of CGM for the measurements of dry mass of mammalian cells.[14] The interest of directly measuring $\delta\ell$ and not ϕ to access cellular dry mass was illustrated, and a detailed study on the precision and trueness of the dry mass measurements was conducted. The authors also addressed an important aspect of dry mass measurements that is cell segmentation, by detailing an effective segmentation algorithm for eukaryotic cells, even in confluence.

All these phase and wavefront microscopy techniques were then used to tackle biological questions related to cell growth and proliferation.[15–27] Measuring dry mass is certainly the main strength of QPM compared with more common microscopy approaches based on fluorescence measurements. QPM lacks specificity but is quantitative, non-invasive and can run for days without inducing photobleaching or phototoxicity to the sample. All these articles also illustrate the interest of accessing cellular dry mass using optical microscopy compared with microelectromechanical techniques [19,28–31]. Surprisingly, measuring DM by phase or wavefront microscopy technique remains elusive for micro-organisms such as bacteria until very recently,[32,33] while the microbiology community would gain a lot if a simple tool would exist to quantitatively monitor the growth rate of micro-organisms under a microscope, and not only within an incubator.

In this article, we use cross-grating wavefront microscopy (CGM) to demonstrate its ability to simply and accurately measure the dry mass of small cells, such as bacteria. We explain how to handle diffraction fringes, inherent to micrometric objects, to avoid possible inaccuracies in the DM estimation. We also quantify the accuracy of the measured dry mass as a function of microscope focus and objective numerical aperture. Then, we introduce the use of the optical polarizability, measured by CGM, as a complementary information to dry mass. Finally, the method is illustrated on two case studies: the monitoring of the dry mass evolution of a microscale colony forming unit and its dependence on temperature, and the use of the optical polarizability as a ratiometric measurement to help classify imaged bacteria.

MATERIALS AND METHODS

Image acquisition using cross-grating wavefront microscopy (CGM)

QLSI, introduced and patented by Primot *et al.* in 2000,[11,34] is based on the use of a 2-dimensional grating (or the synonym, cross-grating) positioned at a millimetric distance from a camera chip.[12] A QLSI cross-grating consists of a $0-\pi$ phase checkerboard pattern that favors the diffraction of only the 1st orders. The measured interferogram enables the computation of both the intensity and wavefront profiles of a light beam, with higher accuracy and definition compared with Shack-Hartman wavefront sensors. When QLSI is implemented on a microscope, a configuration we recently proposed to name cross-grating wavefront microscopy (CGM) for the sake of simplicity, the measured intensity and wavefront profiles become the transmittance and the optical path difference (OPD) of the imaged object, as demonstrated by Bon *et al.* in 2009 for applications in biology.[35] More recently, applications in nanophotonics have been reported by our group to image and characterize nano-objects.[36–39]

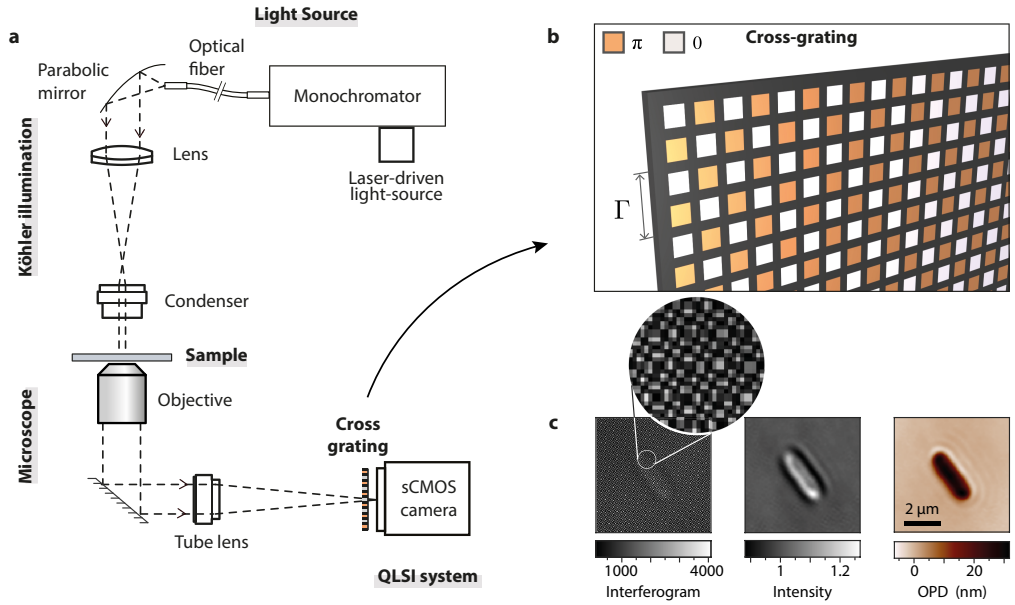

Figure 1: ***Experimental setup for cross-grating wavefront microscopy.*** *(a) Schematic of the microscope. (b) Schematic of the 2D-grating (aka cross-grating) placed at a distance of 0.86 mm from the camera sensor. (c) From left to right, raw camera image called the interferogram, transmittance image, and OPD image, both retrieved from the interferogram.*

The $0-\pi$ phase shift pattern is key to obtain a non-diffractive light wave between the grating and the camera, meaning that the light wave propagates keeping the same pattern. This shadow-like propagation creates an array of dots, the position of which can be precisely determined if they are sampled by at least 3 pixels, in practice. As a consequence, the definition of the QLSI image is reduced by a factor of 3, in the two dimensions of the image, leading to the reduction by a factor of 9 of the total amount of pixels.

All the experiments were conducted on a home-made microscope (Figure 11), composed of a monochromator as a light source (Hypermonochromator, Mountain Photonics GmbH associated with an Energetiq EQ-99X laser-driven light source (LDLS), purchased from Opton Laser International, hyperchromator DG-600-300/1250) mounted in a Köhler configuration. The monochromator was tuned at a wavelength $\lambda = 540$ nm or $\lambda = 625$ nm depending on the experiments. We used Olympus objective lenses (100x - oil - 1.3 NA - UPLFLN100xOP / 100X - oil - variable NA - UPLFLN100xOI2 / 40x - air 0.6 NA LUCPLFN40x / 60x - oil - 1.25NA - UPLFLN60XOI) ; a tube lens with a focal length of 200 mm (Thorlabs, TTL200-A), multiplying the effective magnification of the microscope by a factor of 1.1, compared with the objective's ; a QLSI wavefront imaging system, consisting of a Zyla camera 5.5 and a QLSI cross-gratting of pitch $\Gamma = 39$ µm placed at 0.86mm from the camera sensor.

Sample preparation

Escherichia coli and *Geobacillus stearothermophilus* were usually cultivated in LB medium overnight at 37°C, 200 rpm. *Lactobacillus reuteri* was pre-cultured in MRS medium overnight at 35°C, 200 rpm. *Deinococcus radiodurans* was pre-cultured in TGY2X medium overnight at 30°C, 200 rpm. The archaeon *Sulfolobus shibatae*

was cultivated in 182 medium over 3 days at 75°C, 200 rpm. The bacterial and archaeal concentrations were evaluated by measuring the optical density (OD) of the culture (Ultrospec 10 Cell Density meter biochrom).

Different sample geometries were used depending on the experiment.

For the experiments on the effect of the focus and the numerical aperture: a volume of 5 µL of bacteria with an OD of 0.4 was sandwished between two glass coverslips (Ø25-mm at the bottom and Ø18-mm on the top) and placed in a metallic sample holder (Attofluor™ cell chamber, Thermofisher). After 15 min of sedimentation, the bacteria were imaged using the microscope.

For the experiments related to precision estimation, a volume of 10 µL of bacteria suspension with an optical density of 0.05 was left to dry on a microdish with a glass bottom and 400 µL of LB culture media was added on top. A Ø25-mm glass cover slip was added on top of the medium, to ensure a stable, flat upper interface, not likely to distort the incoming light wavefront. Then, the bacteria were imaged after 30 min of sedimentation.

For the experiments on *E. coli* growth as a function of the temperature, see the section "bacteria heating" below.

Cell heating

For any experiment at higher temperature than the ambient temperature, the bacteria were heated using a micro-heating device (VAHEAT, Interherence GmbH), consisting of a sample holder of the size of a glass slide that contains a glass coverslip in which an electrical current can flow. The heating coming from the glass coverslip directly enables a fast temperature control over a square area of around 5×5 mm^2 at the bacteria location. This small heating device enables a simple and fast control of the temperature (around 1s to reach the temperature target and a few seconds to cool down to room temperature). The experiments were conducted on two types of samples, the Standard Smart Substrates (SmS) and the Standard Smart Substrates with PDMS reservoir (SmS-R). With SmS, a volume of 0.5 µL of bacteria suspension with an OD of 0.05 was deposited on the substrate and covered by the 5×5 mm^2 cover slip to prevent convection. For the SmS-R, the PDMS cuvette was filled with LB culture media, and an extra 25-mm glass coverslip was added on top of the cuvette to prevent evaporation during the experiment and ensure a flat, stable top interface.

Numerical simulations

IF-DDA is a free software that we developed to rigourously solve the problem of electromagnetic scattering of small object in three dimensions.[40] The software can be downloaded from the webpage https://www.fresnel.fr/perso/chaumet/ifdda.html. IF-DDA is based on the discrete dipole approximation (DDA), which is a volume-integral equation method.[41] The principle consists of discretising the object under study in 3D on a cubic mesh, computing the electromagnetic field inside the object, and computing the subsequent light emission by the object through a microscope to get the electromagnetic field at the object plane.

RESULTS AND DISCUSSION

Dry mass δm measurement method

Equations (3) and (4) introduced the calculation method of the OV and DM of an object from its OPD image. In practice, the double integration amounts to summing pixel values over a domain $\mathcal{D}$ of the image:

$$\delta V = p^2 \sum_{i,j \in \mathcal{D}} \delta \ell_{i,j} \,, \tag{7}$$

$$\delta m = \gamma^{-1} p^2 \sum_{i,j \in \mathcal{D}} \delta \ell_{i,j} \,, \tag{8}$$

where p^2 is the pixel area. Provided a good background subtraction is performed, the domain of integration $\mathcal{D}$ is easy to define when considering eukaryotic cells.[14] However, it is *a priori* less obvious to determine when dealing with small objects because of diffraction, which makes the boundaries of the object not well defined. We recently pointed out this issue with the DM measurement of neurites using CGM.[42] Figure 12a displays a simulated OPD image of a bacteria, of the rod-shape of a *E. coli*, obtained using IF-DDA (see Method section). One can see that diffraction rings spread much further than the geometrical size of the bacteria, raising the question of what the proper integration area $\mathcal{D}$ should be to properly calculate the DM δm and OV δV using Eqs. (7) and (8). To numerically answer this question, we calculated the OV of a *E. coli* bacterium as a function of the size of the integration area $\mathcal{D}$ (Figure 12b), and compare with the theoretical value $\delta V = (n - n_0)V$. We define a dilation factor $f = d/d_0$ where d_0 is the width of the bacteria and d is the width of the domain $\mathcal{D}(f)$. The plot of Figure 12b shows that integrating over $\mathcal{D}(f = 1)$, i.e. over the geometrical size of the bacteria, or over what a segmentation algorithm would normally capture, tends to yield inaccurate measurements. Around $f = 1$, the values are slightly underestimated (0.0122 instead of the true value of 0.0131 μm^3), and the slope of $\mathcal{D}(f)$ remains large, making any OV and DM measurement likely to feature a large dispersion of the measurements. Figure 12b also shows that if the diffraction are all captured within the integration area $\mathcal{D}(f)$, the measured DM and OV tend toward the theoretical values (0.0131 μm^3 and 65 fg respectively). Thus, for a proper estimation of DM and OV, the diffraction rings must be all captured.

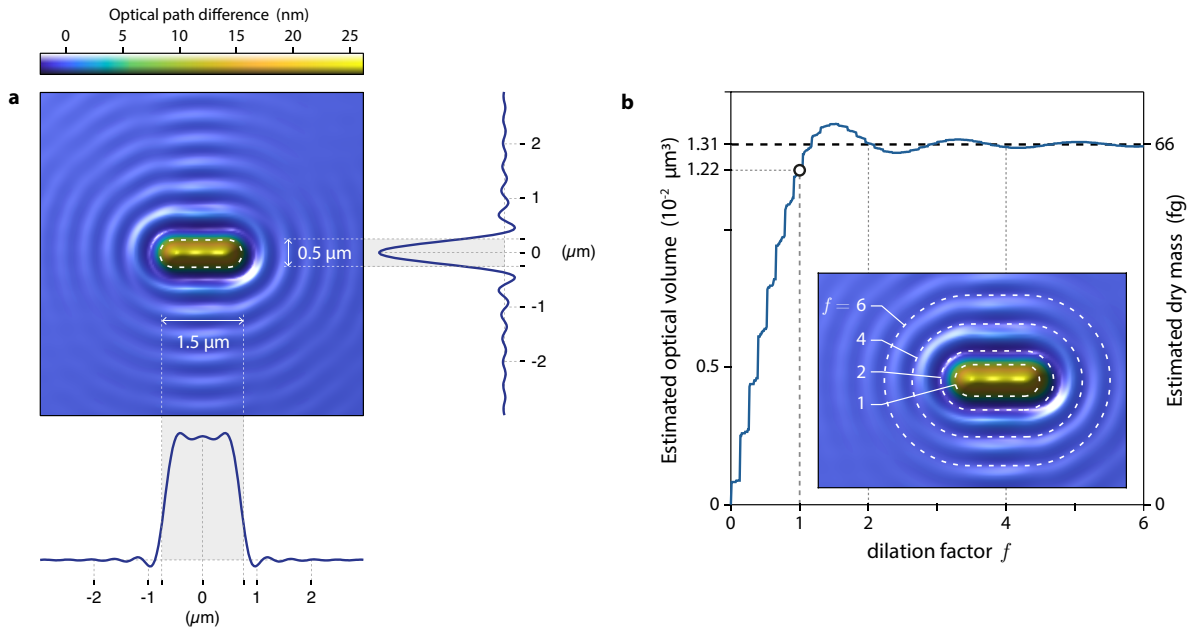

Figure 2: ***IF-DDA numerical simulation of the image of a bacterium****, at focus, on glass in water, modelled as a rod of length 1.5 µm, diameter 0.5 µm and refractive index 1.38 ($\lambda = 550$ nm, 1.3NA). (a) Simulated OPD image of the bacterium along with horizontal and vertical crosscuts passing by the center of the bacterium. The dashed line represents the geometry of the bacteria. (b) Estimated optical volume and dry mass as a function of the dilation factor f of the area over which the image integration is numerically performed. The dashed line represents the theoretical values. The dashed lines in the inset represent the geometries of several integration areas $\mathcal{D}(f)$ for various dilation factors f (1, 2, 4 an 6).*

Experimentally, because these diffraction rings are tenuous, standard segmentation algorithms tend to miss them. For this reason, we recently proposed a refined algorithm aimed to capture them, in the context of neuron imaging.[42] The algorithm, we developed in Matlab and provide on Github,[43] is depicted in Figure 3. It involves a first step of segmentation of the cell, which can be performed using any regular segmentation algorithm. We chose a magic-wand approach where, by clicking on on bacterial cell, the whole body of the bacterium is automatically selected. Then, the selected domain $\mathcal{D}$ is resized by a factor f and the optical volume, calculated over the domain $\mathcal{D}(f)$, is plotted as a function of f. This plot naturally shows an increase of the optical volume as a function of f from $f = 0$ to $f = 1$, until it reaches a plateau corresponding to a proper capture of the diffraction rings, and to the true OV. The plateau is reached at an f value of around 1.5, substantially greater than 1, evidencing the need to capture a larger area than what a regular segmentation algorithm would do. Above $f = 1$, oscillations of the estimated DM are observed due to the diffraction rings, which are barely visible but substantially affect the dry mass estimation.

Caution should be used, though, with experimental OPD images. Unlike simulated images, which naturally exhibit a zero OPD value far from the imaged objects, experimental OPD images are obtained to within an arbitrary additional constant. Indeed, CGM primarily measures *gradients* of OPD, and the OPD image is subsequently obtained by integration of these gradients, which adds an arbitrary constant. To circumvent this specificity of CGM, we neither undertake to adjust the background offset, nor correct any background non-uniformity. Instead, for each estimation of the OV or DM at a particular f value, we simply subtract to the image the average OPD value over the boundary of the segmented area $\mathcal{D}(f)$ (represented by a white area in Figure 3c-e). This method yields a precise and simple estimation of OV and DM, and is not sensitive to the arbirary offset of the OPD and to any non-uniformity of the OPD background. Figure 3f plots the measured OV as a function of the dilation factor f using the methods depited above. Note that image noise can limit the range of f values, as explained futher on in the manuscript.

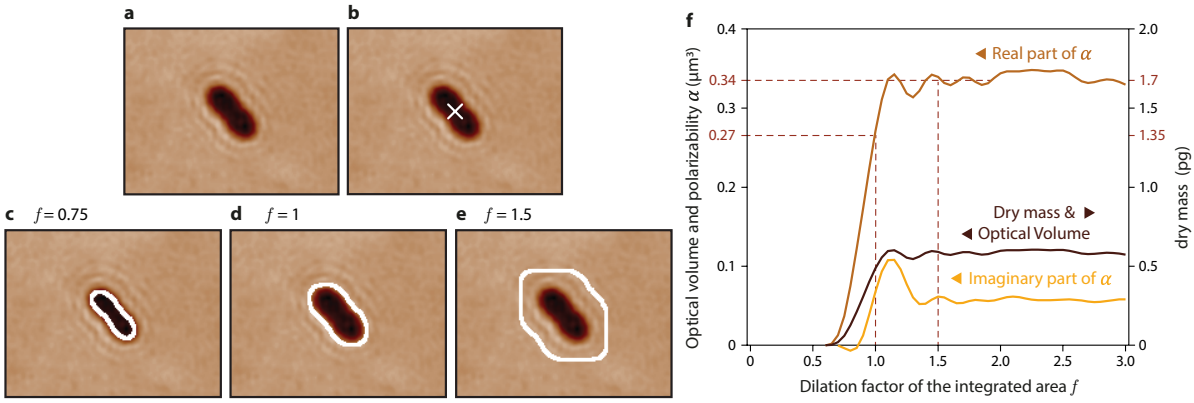

Figure 3: ***Procedure of segmentation for dry mass estimation.*** *(a) Experimental OPD image of a bacterium. (b) Magic-wand selection. (c-e) Segmented areas for various dilation factors f: 0.75, 1 (what the standard segmentation gives) and 1.5 (the minimum segmented area to consider for proper DM estimation). The background value is calcuated over the white, annular area that is 3 px wide. (f) Estimated OV, OP and DM as a function of the dilation factor f.*

As a conclusion, diffraction rings must be taken into account for an accurate measurement of the dry mass. Even if they look tenuous, they contribute to a substantial part of the information. This conclusion is consistent with our recent study on nanoparticles (100 nm in size), even much smaller than bacteria, which were also featuring diffraction rings that must be integrated to yield a proper estimation of the optical complex polarizability of the nanoparticle.[38] The interest of measuring the OV on a plateau of $\delta V(f)$, rather than at $f = 1$, is not only to obtain a value closer to reality. The other, and equally important, interest of expanding the summation area is that the slope of $\delta V(f)$ is weaker (Figure 3f), leading to much less dipersed measurements, and thus more reproducible and precise dry mass estimation.

Optical polarizability α measurements

Besides the OV and DM, we introduce in this article another physical quantity to be measured from the optical images that also contains valuable information: the complex optical polarizability (OP) α.[38] We introduced the ability of CGM to measure this quantity in a previous publication dealing with metallic and dielectric nanoparticles.[38] The optical polarisability α is a complex number that characterizes the optical response of the nanoparticle. Unlike the dry mass or the optical volume, which can be calculated from the sole OPD image, the calculation of α involves a mix of both the intensity (i.e. transmittance) and OPD images, T and $\delta\ell$:

$$\alpha = \frac{i\lambda n_0}{\pi} \iint \left(1 - \sqrt{T(x,y)}\exp(i2\pi\delta\ell(x,y)/\lambda)\right) \mathrm{d}x\mathrm{d}y\,, \tag{9}$$

$$\alpha = \frac{i\lambda n_0 p^2}{\pi} \sum_{i,j\in D} \left(1 - \sqrt{T_{i,j}}\exp\left(i2\pi\delta\ell_{i,j}/\lambda\right)\right), \tag{10}$$

where n_0 is the refractive index of the substrate (usually glass). Compared with δV, α is richer because it also contains information coming from the intensity image. Also, as demonstrated further on, α can give ratiometric measurements, no longer dependent on the bacteria size, and representing a signature of the bacteria type.

The OP has the dimension of a volume, just like the OV. There exists an interesting relation between OP and OV. For $\delta\ell \ll \lambda$ (which is normally the case for bacteria), a Taylor development at the 1st order gives the following expression for the real part of α:

$$\mathrm{Re}(\alpha) \approx -2n_0 p^2 \sum_{i,j\in D} \sqrt{T_{i,j}}\delta\ell_{i,j} \,. \tag{11}$$

For $T \approx 1$ (a good approximation for transparent objects), from Eq. (11), the real part of the OP and the OV becomes proportional:

$$\delta V \approx -\mathrm{Re}(\alpha)/(2n_0) \,. \tag{12}$$

In addition to having the same dimension, the OP and OV have thus the same order of magnitude.

From Eqs. (11) and (12), one can define the weighted OV δV_w, defined from the OPD image weigthed by the transmittance image:

$$\delta V_w \approx \sum_{i,j\in D} \sqrt{T_{i,j}}\delta\ell_{i,j} \,. \tag{13}$$

Because δV_w is defined from the OP which tends to be focus-independent,[38] we shall see in the next section that considering the weighted OV δV_w (Eq. (13)) instead of normal δV (Eq. (7)) makes the estimation of the OV, and thus the DM, less focus dependent, and more precise.

Validity of DM measurements as a function of the object size

Equation (2), and all the following equations used to determine OV and DM, suppose the projective approximation. This approximation is no longer valid in the case of small particles, where ray optics no longer applies. Nanoparticle can even feature plasmonic or Mie resonances, making the measured OV far from being only dependent on the volume of the object, because surface effects dominate bulk properties. The question of whether dry mass measurements can be performed on nano-objects is thus relevant. In this section, we conduct DDA simulations to investigate the accuracy of OV measurements as a function of the object size. We chose to consider objects that vary progressively from a 50-nm sphere (corresponding to a virus or a vesicle) to a 4x2 µm elongated rod (corresponding to a large bacteria), immersed in water, lying on glass. The refractive index of the objects was kept at 1.38, a typical value for cells. We also varied the focus from -0.5 to 0.5 µm, for each object. Results are plotted in Figure 14. In each simulated OPD image, a pixel summation (Eq. (7)) was performed to determine the so-called imaged OV (red solid lines). The main observation is that OV and DM measurements can be safely conducted even for the smallest objects. In particular, for small objects, measured and theoretical OV line shapes are indistinguishable (first 3 graphs of Figure 14). There is just a weak

dependence of the imaged OV as a function of the focus, in particular for large objects, which makes the OV measurements less accurate when the microscope is defocused. This focus dependance is studied in more detail in the next section. The conclusion here is that dry mass measurements can be safely conducted for arbitrarily small biological objects.

We stopped here the simulation at a minimum size of 50 nm, because it would be difficult to image objects smaller than that using any QPM. Note that using interferometric scattering (iSCAT), it is possible to detect single proteins, and if a proper calibration is performed, it is even possible to determine their mass.[44]

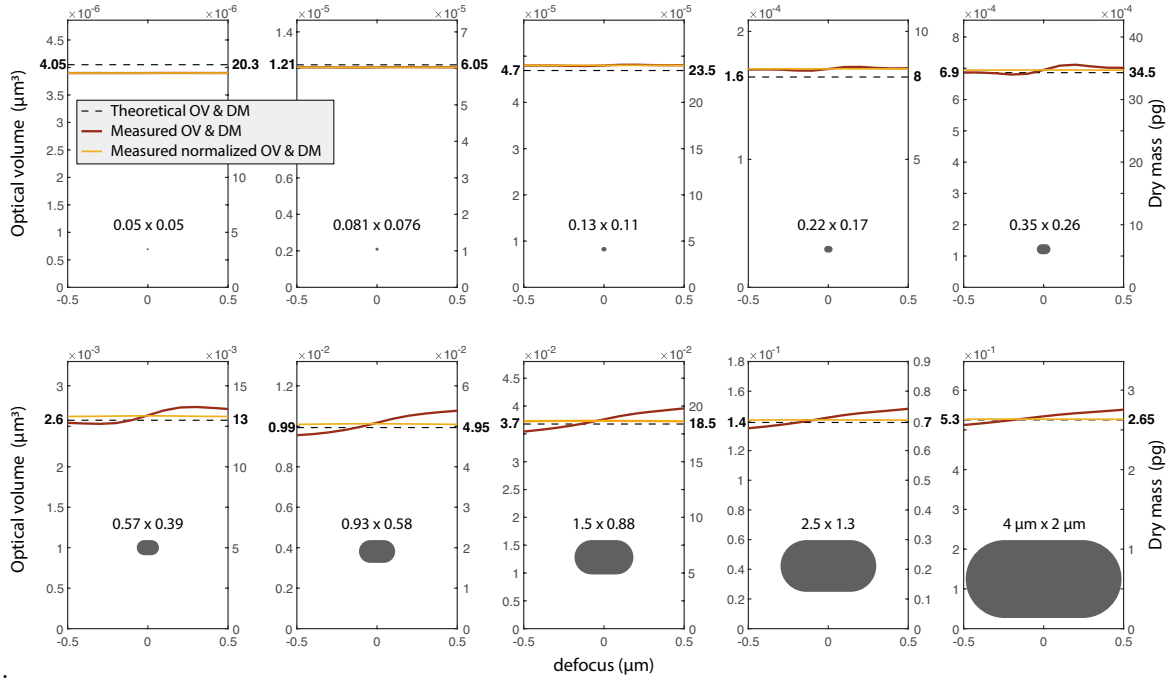

Figure 4: ***Optical volume and dry mass measured on numerical OPD images of 10 micro-objects, simulated using IF-DDA, as a function of the microscope focus.*** *The morphologies span progressively from a 50-nm sphere to a 4 µm x 2 µm rod. The objects feature a refractive index of $n = 1.38$, are deposited on glass (1.51) and immersed in water ($n_0 = 1.33$). In each case, a drawing of the object is inserted, specifying the dimensions of the object. The dashed lines represent the theorietical OV. The red (darker) lines represent the OV and DM measured on the OPD images by pixel summation, according to Eq. (7) and Eq. (8). The yellow lines represent the weighted OV and DM measured on the OPD images by pixel summation, according to Eq. (13).*

Influence of image noise on the measurements of δm and α

The primary source of noise in CGM is the shot noise (aka photon noise).[13] Thermal or reading noise can be considered as negligible because the intensity on the camera sensor in CGM is normally high. This shot noise creates a white noise on the interferogram and on the measured wavefront gradients. Upon integrating the wavefront gradients to get the OPD image, this white noise turns into a Brown noise (or Flicker noise).[13] While white noise features a uniform spectral distribution, a Brown noise is

characterized by a spectral distribution in $1/F^2$ (the inverse of spatial frequency squared), meaning that low frequencies are particularly important in the noise of OPD images in CGM.

In order to investigate the effect of this particular noise on DM and OP measurements, we conducted numerical simulations. We simulated flat images endowed with a Brown noise, where we fixed the noise standard deviation at $\sigma_0 = 0.17$ nm, a typical value in CGM. The OV on this image was estimated using Eq. (8), over a circular area of radius R, as defined in Figure 15a. Of course, the OV is supposed to be zero because no object is imaged (float OPD). It is true in average, but not for each particular image due to noise. Figure 15b plots the calculated OV as a function of R using the procedure described in Figure 3. Counterintuitively, although the noise has an averaged value of zero over the image, integrating the noise leads to a divergence of $\delta V(R)$ when increasing R (Figure 15b). We calculated the standard deviation σ_{OV} of the calculated OV for a large set of noise images (5000 noise images), and found a law scaling as $\sigma_{\mathrm{OV}} \sim R^2$ (Figure 15c). This divergence comes from the fact that the noise is a Brown noise, dominated by low spatial frequencies. For a white noise, the divergence would be less dramatic, scaling as R. However, as far as the scaling law is not faster than R^2, the OV of an imaged object also scale as R^2. It means that if the signal of the imaged object is larger than the noise, its dry mass could be measured no matter the object's size. The same conclusion and scaling law apply for the estimation of α.

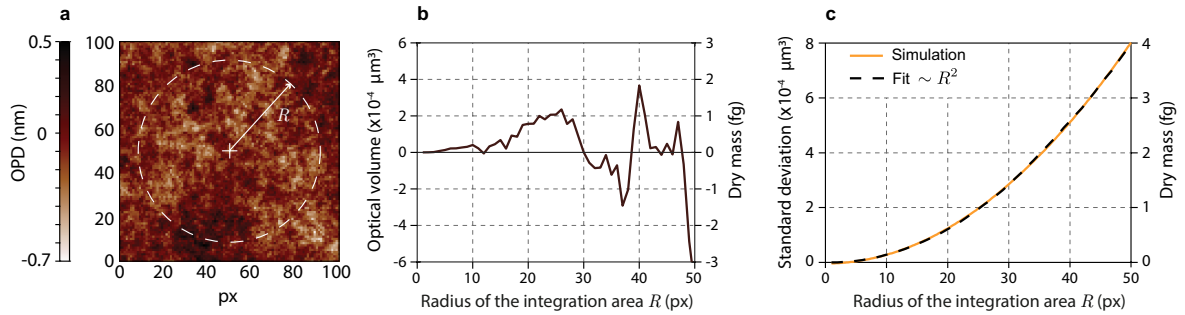

Figure 5: ***Application of the dry mass estimation algorithm on a noise image.*** *(a) Simulated OPD noise image (100x100 px). The integration domain $\mathcal{D}$ consists of a disc of radius R. OV and DM estimated using Eqs. (7) and (8) over $\mathcal{D}$ as a function of R. (c) Standard deviation of the measured OV and DM over 5000 noise images, as a function of R, and fit of the profile by the function $R \to \alpha R^2$.*

Figure 16 further illustrates the effect of the noise of OPD images on dry mass and polarizability measurements, with the OV measurement on a single bacterium, with a common size (optical volume of around 0.2 µm^3). The measured OV and optical polarizability are plotted as a function the integration radius R, both for a bare field of view (Figure 16a) and with the bacterium (Figure 16b). From this comparison, one can see that the effect of the noise becomes detrimental from $R \sim 90$ px, much further than the onset of the plateau at $R \sim 50$ px (see Figure 16b) where the measurements should be done.

Thus, for bacteria, and more generally for anything that stands out from the noise, precise OV and OP measurements can be done. Things are more difficult when dealing with nanoparticles for instance. Gold nanoparticles, 100 nm in diameter, could be precisely characterized for instance, with normal imaging conditions (averaging of 30 interferograms). For smaller objects, like vesicles of viruses for instance, the estimation of the dry mass could be more difficult, but can always be improved by averaging more interferograms. A detailed description of the noise of OPD images acquired using CGM, and on how to minimize it, is provided in Ref. 13.

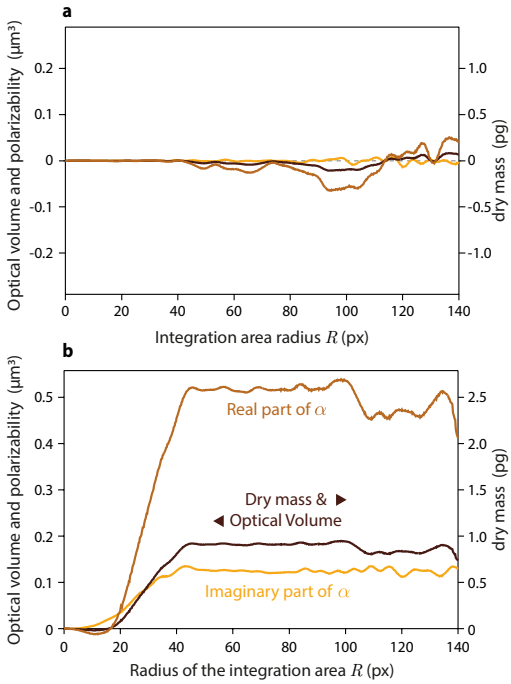

Figure 6 : Optical polarizability, optical volume and dry mass as a function of the integration radius, (a) without any object on the image (only noise), and (b) in the presence of a bacterium.

Dependence of δm and α measurements on focus and numerical aperture

Changing the focus of the microscope strongly affects the intensity and OPD images, from which the OV, DM and OP are calculated. The imaged objects look more blurred when the microscope is defocused. It is thus important to determine to what extent the focus affects the estimations of these quantities. The focus is indeed not straightforward to determine and can vary from one image to another. When visually adjusting the focus of a microscope, what is perceived as the right focus can be user-dependent and, as a more subtle problem, the right focuses usually look much different when looking at the intensity or OPD images. Because of this uncertainty, it is important to determine the focus range that yields reproducible values of OV, DM and OP. A similar issue is *a priori* possible with

335 the numerical aperture (NA) of the microscope, which affects the image in the same manner as the
336 focus.
337 The case of the dependence of DM on the focus has been studied using CGM with eukaryotic cells by
338 Aknoun et al.,[14] who showed that the measured DMs do not vary more than 1% if the defocus remains
339 within ±5 μm. This weak dependence comes from the fact that refraction and diffraction are negligible
340 for eukaryotic cells. The authors also showed that the NA does not affect the cells dry mass
341 measurements at all. Since bacteria are much smaller than eukaryotic cells, and their OPD images more
342 affected by diffraction and more dependent on the focus and the NA, these rules derived for eukaryotic
343 cells should be reconsidered for bacteria.
344 Regarding the OP α, we demonstrated in a previous publication that its estimation is supposed to be
345 rigourously independent on the focus and NA, if the surrounding medium is uniform.[38] However, cells
346 in culture lie at the vicinity of a glass/water interface, making the surroundings not uniform. The OP α
347 is thus no longer supposed to remain constant in theory.
348 To quantify the effect of the focus and NA on the estimation of OV, DM and OP of objects as small as
349 bacteria, we conducted numerical and experimental studies, presented below.
350 Figure 14 displays numerical simulations of the OV of nano- and micro-objects as a function of the
351 focus of the microscope, from -0.5 to 0.5 μm. These simulations evidence a slight dependence of OV
352 on the focus, especially for large objects (not for nanoparticles). However, OV variations remains
353 confined within 10% maximum if the focus is varied by ±0.5 μm. This range of variation does not
354 preclude OV measurements. Interestingly, using the normalized OV defined by Eq. (13) enables the
355 cancellation of this dependence, for any size of the imaged object, and the estimation of the proper
356 OV. The use of the intensity-normalized OV appears thus as an effective way to limit the dispersion of
357 OV measurements. Note that these simulations do not specifically concerns CGM. These results apply
358 for any QPI.
359 To investigate the effect of the focus, we also conducted experiments, on *E. coli* bacteria. Bacteria
360 cultures were imaged at room temperature, not at the optimal growth temperature of 37°C. This way,
361 the bacteria did not grow over the duration of the experiment to ensure that variations of the measured
362 dry masses from one image to another do not come from actual dry mass variations.

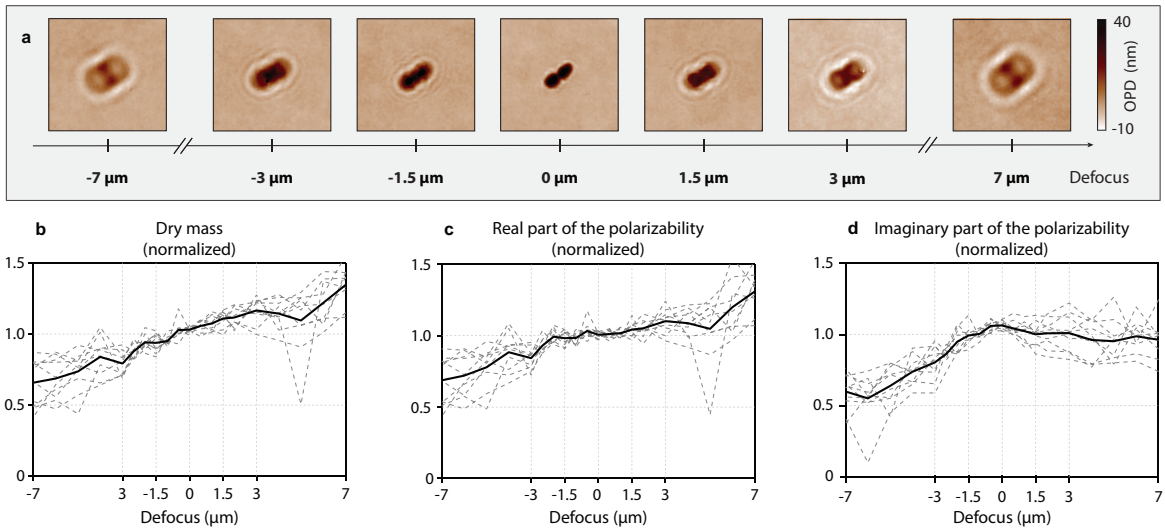

The focus was varied from -7 µm to +7 µm. This wide range of values is purposely exaggerated as a means to better cover the subject. In practice, for bacteria, the focus can be visually set within a range of ±1 µm with a good reproducibility (see Figure 17a). Figure 17b-d demonstrate a substantial effect of the focus on the measured OV and α values. Unlike eukaryotic cells that demonstrate a parabolic dependence of the measured δm values as a function of the focus,[14] we found a linear dependence for bacteria. However, subtantial deviation of δm and α are only observed for defocuses that can be easily avoided experimentally. Within the more reasonable range of ±1.5 µm, both the OP and OV can be considered constant. Caution should therefore be taken when measuring these optical parameters, the focus should remain in the [-1.5, 1.5] µm range to ensure accurate values of the OV, DM and OP.

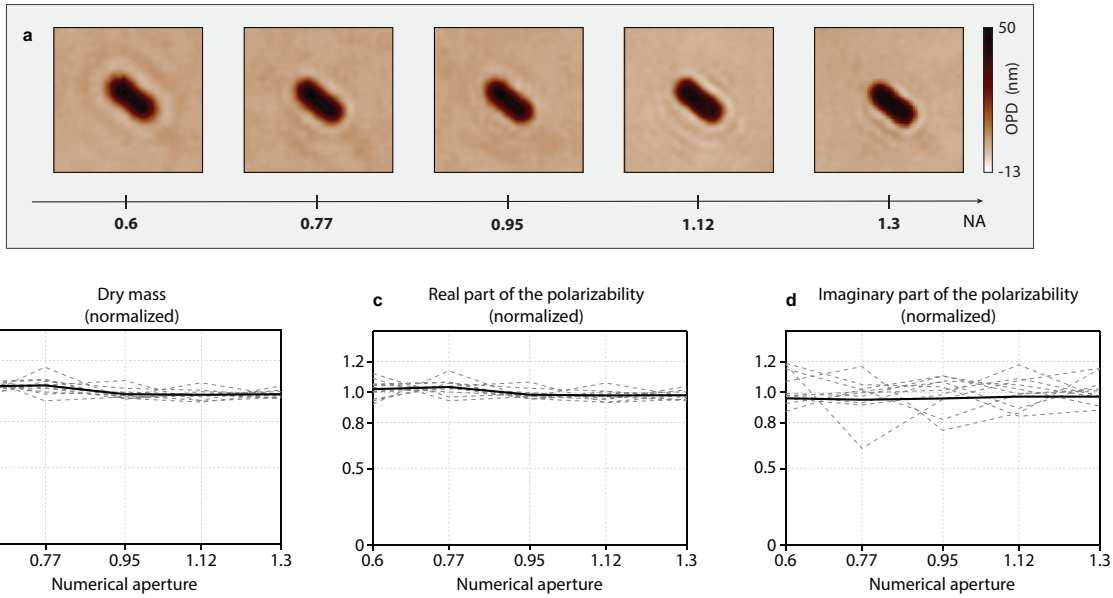

We also conducted a similar study to analyze the influence of the objective NA on the DM δm and the OP α measurements. Figure 18 displays the normalized OV and the normalized real and imaginary

parts of the OP as a function of the objective NA from 0.6 to 1.3. The NA of the objective has no influence on the measurement of the optical volume and the optical polarizability. No caution should be taken regarding the objective NA when conducting dry mass measurements using CGM. The same conclusion was reported for the DM of eukaryotic cells,[14] and for the OP of nanoparticles.[38]

Precision of the measurements

To estimate the precision of OV and DM measurements on bacteria, we acquired a series of 60 successive images on a given set of 10 bacterial cells, and measured the OV of all these cells on all these images using the algoritm depicted in Figure 3. One frame was acquired (no image average), and the measured noise amplitude on the images was 0.72 nm (measured on an empty field of view, 431×450 pixels). This noise level is common in CGM, and can be improved by averaging more OPD images. These 600 OV measurements are presented in Figure 19. For each bacteria, box plots are displayed, giving the average OV along with the standard deviation. The precision, defined as the standard deviation divided by the OV, calculated over the 600 bacteria measurements, is close to 3% (Figure 19).

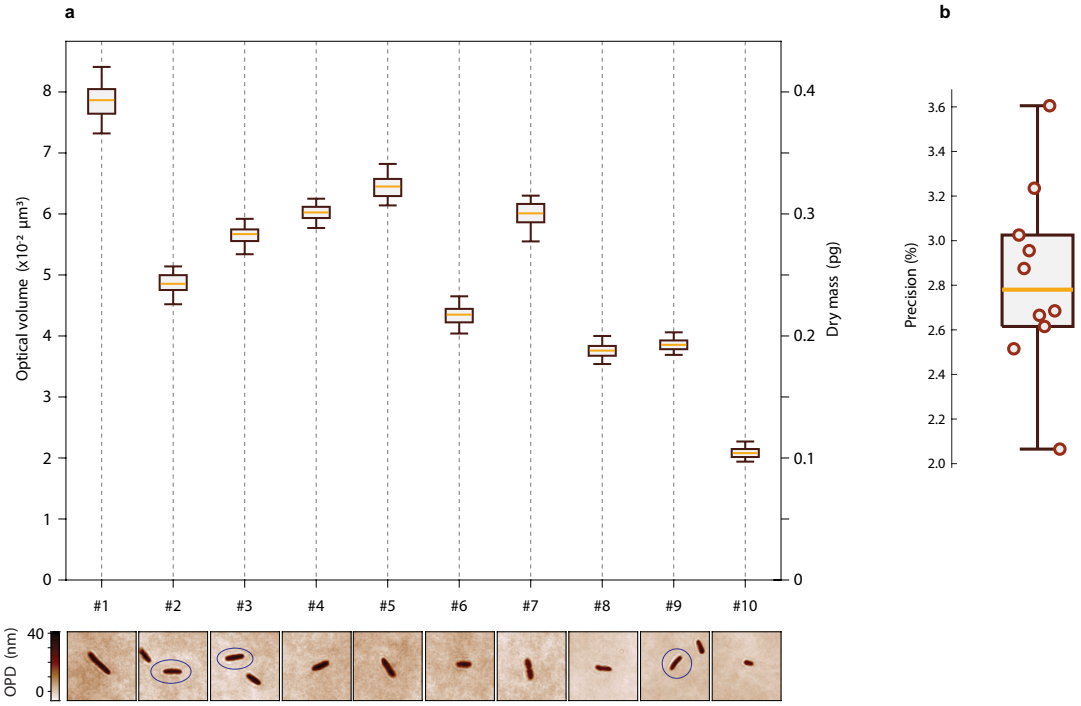

Figure 7 : ***Study of the precision of dry mass measurements.*** *(a) Optical volume and dry ass measurements for 10 different E. coli bacterial cells, 60 measurements each, represented as box plots. (b) Relative standard deviation of these 10 particular bacteria (100x, 1.3NA, λ=530 nm, exposure time 1s).*

Concept of microscale colony forming units (mCFU)

Dry mass metrology using QPM represents a powerful tool to quantitatively measure the growth rate of cells in culture. Their successive replications of procaryotic cells can yield the formation of groups of

cells in close vicinity (clusters or chains), making segmentation and dry mass estimations of single cells complicated. Nevertheless, to properly estimate the growth rate of a bacteria/archaea population using QPM, it makes sense to follow the mass of a group of cells originating from a single one. Such a cell agglomeration is thus not problematic, on the contrary. We call it a microscale colony-forming unit (mCFU), in reference with CFU that are visually observed in petri dishes, at the macroscale.[45]

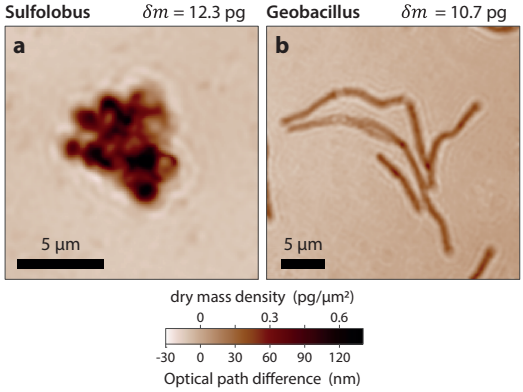

Figure 8 : ***Examples of microscale colony forming units (mCFU).*** *(a) mCFU of the Sulfolobus shibatae archaeon. (b) mCFU of the Geobacillus stearothermophilus bacterium. The measured dry masses of the mCFUs are indicated on top of the images. (60x, 1.25NA, λ=625 nm).*

Examples of applications

Monitoring of the growth rate of bacteria over time

As an illustration of the methods and concepts introduced in the previous section, related to dry mass measurements using CGM, we present here results related to the growth of *E. coli* over time followed by CGM. We followed in real time the bacteria proliferation and quantified the growth rate by monitoring the dry masses of several mCFU over time. The bacteria were incubated at their optimum growth temperature of 37°C. The bacterial cells were imaged using a $40\times$ air objective, at $\lambda = 625$ nm. An image sequence was acquired for >5 h to capture the growth of several mCFUs originating from single bacteria. Figure 21 plots the average of the DM evolution for 5 different mCFUs, in both normal scale (a) and semi-logarithmic scale (b). An exponential growth is observed, followed by a plateau after 4 hours corresponding to the expected stationary phase reached when the bacterial cell density is too high. The data were fitted using an exponential function $m = m_0\, 10^{t/\tau} + \text{cst}$, where $g = 1/\tau$ is the growth rate (number of division per unit time). The growth rate at 37°C was found to be $g = 0.71$ h^{-1}, which is consistent with culture conditions used in this study

In all these measurements on mCFU, we used the same procedure as the one described for single bacteria, involving a dilation factor and a plateau (Figure 5).

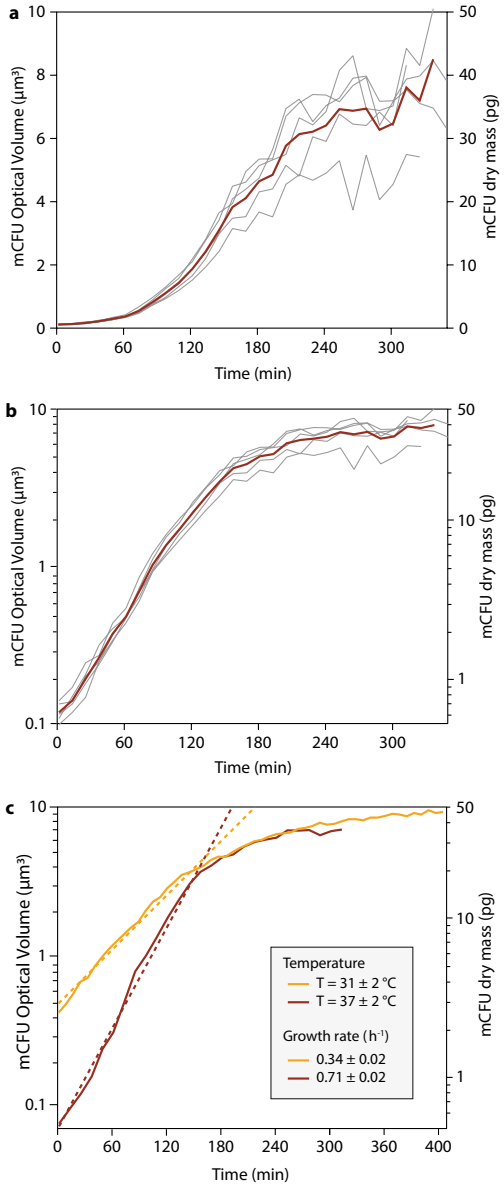

Figure 9 : (a) Dry mass evolution of 5 E. coli mCFUs cultured at 37°C along with the averaged plot. (b) Same data as (a) in a semi-log scale. (c) Dry mass evolution of 2 E. coli mCFUs cultured at 31°c and 37°C. 40x air objective, λ=625 nm.

We take the opportunity here to show how CGM, coupled with a fast micro-heating system (VAHEAT, Interherence GmbH), can be conveniently used to investigate the effect of the temperature on the growth rate of micro-organisms. Figure 21 presents results on the growth of *E. coli* at two temperatures, namely 31 and 37°C. The dry mass evolution of mCFUs is presented in a semi-log scale in Figure 21c to better evidence the exponential growth, corresponding here to a linear trend. In both cases, the dry mass exponentially increases over time before reaching a stationary phase for both temperatures. Faster bacterial growth is observed at 37°C compared to 31°C, as expected, and this variation could be quantitatively estimated; 0.71 h^{-1} at 37°C and 0.34 h^{-1} at 31°C. This is in agreement with previously

reported values from the literature.[46] The bacterial growth rate slowly increases until its optimum temperature 37°C then drops for temperature higher than 37°C.

Toward the differenciation of bacteria using α measurements

The complex optical polarizability (OP) α of a particle is of utmost interest when the particle is used for its optical properties: α contains all the information related to its interaction with light (e.g., scattering and absorption properties). CGM appears thus as a precious metrology tool in nanophotonics. However, for bacteria, the interest of α is not as straightforward, because one is not particularly interested in their optical properties. Here, we show to what extent α measurements can represent nevertheless an interesting approach in biology, to enrich phase or wavefront images of bacteria.

The specificity of the OP is that it combines not only two images (intensity and OPD), but also two numbers: its real and imaginary parts. Just like the dry mass, these two numbers scale as the cell volume. Thus, by taking their ratio, the argument of α, or any other such combination, one ends up with a dimensionless quantity that no longer depends on the volume of the bacteria, but on its nature. Combining intensity and phase images to obtain alpha enables thus the derivation of ratiometric measurements, and possibly to a new method to discriminate different procaryotic species with similar phenotypes. We investigated this possibility by screening experiments on 4 different bacteria species, namely *E. coli, Geobacillus stearothermophilus, Deinococcus radiodurans and Lactobacillus reuteri*. Results are gathered in Figure 22. We chose to plot the argument of complex polarizability $\arg(\alpha)$ as a ratiometric, volume-independent quantity. The results show that different species can exhibit different average α values. $\arg(\alpha)$ appears as a balance between absorption and refraction. What would make $\arg(\alpha)$ (or any other ratiometric quantity) different from one bacterial species from another is thus different ratios of absorption coefficient and refractive indices. More sophisticated ratiometric quantitities could be designed to possibilty make the measurements less dispersed and make this method more efficient for a better identification.

The results presented in Figure 22 are not convincing enough to be used to differentiate micro-organisms: the data look dispersed and the difference in $\arg(\alpha)$ from one species to another is not blatant. However, there is a difference and the results presented here highlight a more general concept: the interest of considering also the intensity image, and not only the OPD image, to gain information on the imaged cells. For instance, the group of Park recently developed a deep-learning approach to identify bacterial species but just from phase images, not on intensity ones.[32] Our results suggest here that feeding the artificial neural network (ANN) with, not only phase or OPD images, but also with the corresponding intensity images could markedly improve the ability of ANN to classify objects imaged with phase and wavefront microscopy techniques. Results presented in Fig. 12 could

be more convincing by investigating a more complex ratiometric measurements than simply $\arg(\alpha)$, but also by letting a ANN finding its self the optimized combination.

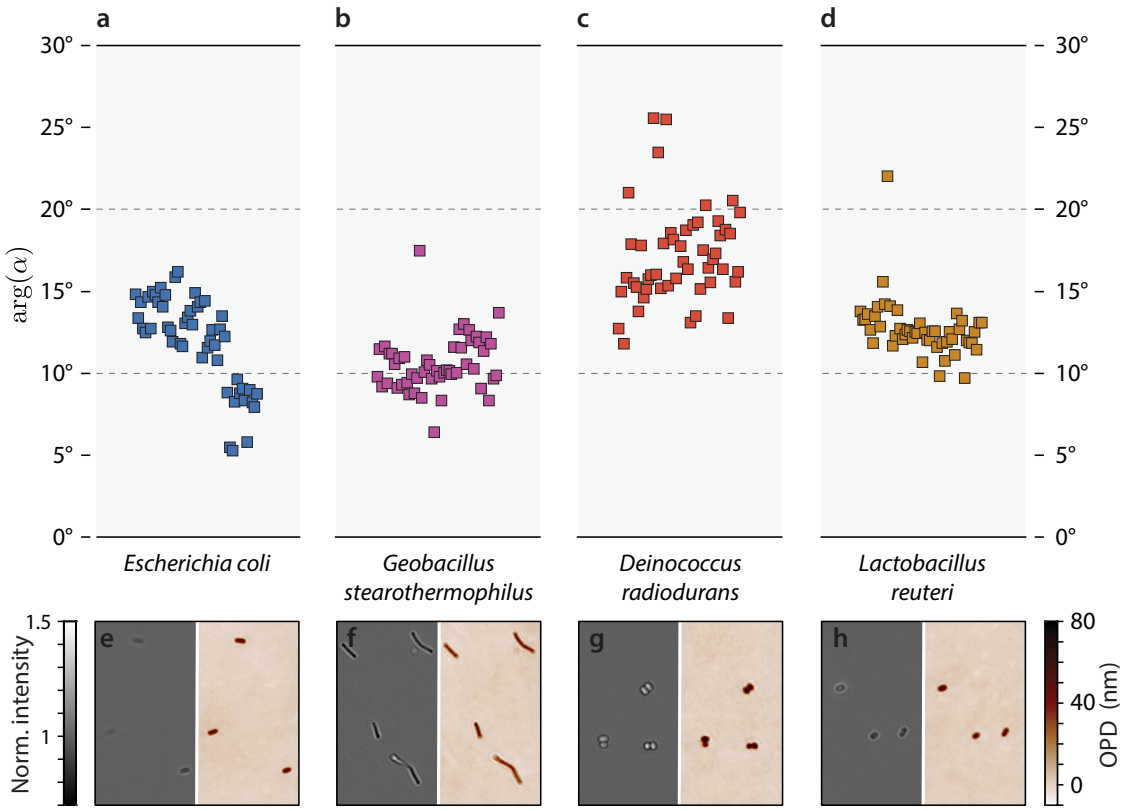

Figure 10: Complex optical polarizability measurements using CGM for various types of bacteria, namely (a) Escherichia coli, (b) Geobacillus stearothermophilus, (c) Deinococcus radiodurans and (d) Lactobacillus reuteri. (e f, g, h) Examples of OPD images associated with these 4 bacteria species.

Conclusion

Dry-mass photometry of bacteria using phase or wavefront microscopy demands a careful control of diffraction, image noise and focus to achieve accurate measurements. We provide numerical tools and experimental rules to achieve accurate dry mass measurements of micro-organisms, and illustrate these approaches by measurements obtained using cross-grating wavefront microscopy.

In addition to the well-known dry mass (DM), and the optical volume (OV) from which it is derived, we introduce two other physical quantities that expand the toolbox for micro-organism characterization using quantitative phase and wavefront microscopies: the weighted OV, and the complex optical polarizability (OP). The weighted OV, computed from the OPD image normalized by the square root of the intensity image, gives rise to OV and DM measurements that are no longer dependent on the focus, leading to more precise measurements. The complex OP has been introduced a few years ago in the context of nanophotonics to derive their optical properties. We show here that useful quantities

can be derived from the OP, such as the argument of the OP supposed to be size-independent, and only dependent only on the nature of the micro-organism.

This article is aimed to pave the way for more accurate dry mass measurement of small biological objects, such as micro-organisms, organelles, vesicles or virions, and expands the functionalities of phase/wavefront microscopy to capture original features that can help the development of refined deep learning algorithms aimed at classifying bacteria.

Although demonstrated using cross-grating wavefront microscopy, the results and techniques describes in this article can be applied to any QPI.

Author contributions

G.B. conceived the project; M.B. prepared the samples, conducted the experiments and analyzed the data; A.G., V.dC. and P.F. trained M.B. for the culture of micro-organisms and provided their expertise in microbiology all along the project; B.M. developed and adapted the program to pilot the experimental setup, and assisted M.B. in the conduction of the experiments; G.B. run the simulations using IFDDA, in close collaboration with P.C.C. and A.S. who developed this code. M.B. and G.B. wrote the manuscripts with input from all authors.

Acknowledgements

This project received funding from the European Research Council (ERC) under the European Union's Horizon 2020 Research and Innovation Programme (grant agreement no. 772725, project HiPhore).

Declaration of interest

The authors declare no conflict of interest

References

1. Barr, E. S. Concerning Index of Refraction and Density. *Am. J. Phys.* **23**, 623–624 (1955).
2. Barer, R. Refractometry and Interferometry of Living Cells. *J Opt Soc Am* **47**, 545–556 (1957).
3. Gul, B., Ashraf, S., Khan, S., Nisar, H. & Ahmad, I. Cell refractive index: Models, insights, applications and future perspectives. *Photodiagnosis Photodyn. Ther.* **33**, 102096 (2021).
4. Khan, R., Gul, B., Khan, S., Nisar, H. & Ahmad, I. Refractive index of biological tissues: Review, measurement techniques, and applications. *Photodiagnosis Photodyn. Ther.* **33**, 102192 (2021).
5. Wientzeck, C., Brohl, H. & Bereiterhahn, J. Dertermination of cellular dry mass by automatic micro-interferometry. *Microscopica Acta* 155–160 (1979).
6. Zicha, D. & Dunn, G. A. An image processing system for cell behaviour studies in subconfluent cultures. *J. Microsc.* **179**, 11–21 (1995).

7. Popescu, G. *et al.* Optical imaging of cell mass and growth dynamics. *Am. J. Physiol.-Cell Physiol.* **295**, C538–C544 (2008).
8. Rappaz, B. *et al.* Noninvasive characterization of the fission yeast cell cycle by monitoring dry mass with digital holographic microscopy. *J. Biomed. Opt.* **14**, 034049 (2009).
9. Mir, M. *et al.* Optical measurement of cycle-dependent cell growth. *Proc. Natl. Acad. Sci.* **108**, 13124–13129 (2011).
10. Girshovitz, P. & Shaked, N. T. Generalized cell morphological parameters based on interferometric phase microscopy and their application to cell life cycle characterization. *Biomed. Opt. Express* **3**, 1757–1773 (2012).
11. Primot, J. & Guerineau, N. Achromatic optical interferometer with continuously adjustable sensitivity. (2000).
12. Baffou, G. Quantitative phase microscopy using quadriwave lateral shearing interferometry (QLSI): principle, terminology, algorithm and grating shadow description. *J. Phys. Appl. Phys.* **54**, 294002 (2021).
13. Marthy, B. & Baffou, G. Cross-grating phase microscopy (CGM): In silico experiment (insilex) algorithm, noise and accuracy. *Opt. Commun.* **521**, 128577 (2022).
14. Aknoun, S. *et al.* Living cell dry mass measurement using quantitative phase imaging with quadriwave lateral shearing interferometry: an accuracy and sensitivity discussion. *J. Biomed. Opt.* **20**, 126009 (2015).
15. Sridharan, S., Mir, M. & Popescu, G. Simultaneous optical measurements of cell motility and growth. *Biomed. Opt. Express* **2**, 2815 (2011).
16. Phillips, K. G., Jacques, S. L. & McCarty, O. J. T. Measurement of Single Cell Refractive Index, Dry Mass, Volume, and Density Using a Transillumination Microscope. *Phys. Rev. Lett.* **109**, 118105 (2012).
17. Cooper, K. L. *et al.* Multiple phases of chondrocyte enlargement underlie differences in skeletal proportions. *Nature* **495**, 375–378 (2013).
18. Sung, Y. *et al.* Size homeostasis in adherent cells studied by synthetic phase microscopy. *Proc. Natl. Acad. Sci.* **110**, 16687–16692 (2013).
19. Zangle, T. A. & Teitell, M. A. Live-cell mass profiling: an emerging approach in quantitative biophysics. *Nat. Methods* **11**, 1221–1228 (2014).
20. Cintora, P., Arikkath, J., Kandel, M., Popescu, G. & Best-Popescu, C. Cell density modulates intracellular mass transport in neural networks. *Cytometry A* **91**, 503–509 (2017).
21. Park, H. S., Ceballos, S., Eldridge, W. J. & Wax, A. Invited Article: Digital refocusing in quantitative phase imaging for flowing red blood cells. *APL Photonics* **3**, 110802 (2018).
22. Tolde, O. *et al.* Quantitative phase imaging unravels new insight into dynamics of mesenchymal and amoeboid cancer cell invasion. *Sci. Rep.* **8**, 12020 (2018).
23. Kandel, M. E. *et al.* Cell-to-cell influence on growth in large populations. *Biomed. Opt. Express* **10**, 4664 (2019).
24. Midtvedt, D., Olsén, E., Höök, F. & Jeffries, G. D. M. Label-free spatio-temporal monitoring of cytosolic mass, osmolarity, and volume in living cells. *Nat. Commun.* **10**, 340 (2019).
25. Sandoz, P. A., Tremblay, C., van der Goot, F. G. & Frechin, M. Image-based analysis of living mammalian cells using label-free 3D refractive index maps reveals new organelle dynamics and dry mass flux. *PLOS Biol.* **17**, e3000553 (2019).
26. Ayyappan, V. *et al.* Identification and Staging of B-Cell Acute Lymphoblastic Leukemia Using Quantitative Phase Imaging and Machine Learning. *ACS Sens.* **5**, 3281–3289 (2020).
27. Aknoun, S. *et al.* Quantitative phase microscopy for non-invasive live cell population monitoring. *Sci. Rep.* **11**, 4409 (2021).
28. Park, K. *et al.* 'Living cantilever arrays' for characterization of mass of single live cells in fluids. *Lab. Chip* **8**, 1034 (2008).
29. Bryan, A. K., Goranov, A., Amon, A. & Manalis, S. R. Measurement of mass, density, and volume during the cell cycle of yeast. *Proc. Natl. Acad. Sci.* **107**, 999–1004 (2010).
30. Godin, M. *et al.* Using buoyant mass to measure the growth of single cells. *Nat. Methods* **7**, 387–390 (2010).
31. Park, K. *et al.* Measurement of adherent cell mass and growth. *Proc. Natl. Acad. Sci.* **107**, 20691–20696 (2010).
32. Kim, G. *et al.* Rapid species identification of pathogenic bacteria from a minute quantity exploiting three-dimensional quantitative phase imaging and artificial neural network. *Light Sci. Appl.* **11**, 190 (2022).

33. Shin, J., Kim, G., Park, J., Lee, M. & Park, Y. Long-term label-free assessments of individual bacteria using three-dimensional quantitative phase imaging and hydrogel-based immobilization. *Sci. Rep.* **13**, 46 (2023).
34. Primot, J. & Guerineau, N. Extended Hartmann test based on the pseudoguiding property of a Hartmann mask completed by a phase chessboard. *Appl. Opt.* **39**, 5715–5720 (2000).
35. Bon, P., Maucort, G., Wattellier, B. & Monneret, S. Quadriwave lateral shearing interferometry for quantitative phase microscopy of living cells. *Opt. Express* **17**, 13080–13094 (2009).
36. Khadir, S. *et al.* Optical Imaging and Characterization of Graphene and Other 2D Materials Using Quantitative Phase Microscopy. *ACS Photonics* **4**, 3130–3139 (2017).
37. Khadir, S., Chaumet, P. C., Baffou, G. & Sentenac, A. Quantitative model of the image of a radiating dipole through a microscope. *J. Opt. Soc. Am. A* **36**, 478 (2019).
38. Khadir, S. *et al.* Full optical characterization of single nanoparticles using quantitative phase imaging. *Optica* **7**, 243 (2020).
39. Khadir, S. *et al.* Metasurface Optical Characterization Using Quadriwave Lateral Shearing Interferometry. *ACS Photonics* **8**, 603–613 (2021).
40. Chaumet, P. C. *et al.* IFDDA, an easy-to-use code for simulating the field scattered by 3D inhomogeneous objects in a stratified medium: tutorial. *J. Opt. Soc. Am. A* **38**, 1841 (2021).
41. Chaumet, P. C. The Discrete Dipole Approximation: A Review. *Mathematics* **10**, 3049 (2022).
42. Durdevic, L., Relaño Ginés, A., Roueff, A., Blivet, G. & Baffou, G. Biomass measurements of single neurites in vitro using optical wavefront microscopy. *Biomed. Opt. Express* **13**, 6550 (2022).
43. Bénéfice, M. & Baffou, G. github.com/baffou/CGM_magicWandSegmentation. (2022).
44. Young, G. *et al.* Quantitative mass imaging of single molecules. *Science* **360**, 423–427 (2018).
45. Molinaro, C. *et al.* Life at high temperature observed in vitro upon laser heating of gold nanoparticles. *Nat. Commun.* **13**, 5342 (2022).
46. Noor, R., Islam, Z., Kishore, M. & Rahman, F. Influence of Temperature on Escherichia coli Growth in Different Culture Media. *J. Pure Appl. Microbiol.* **7**, 899–904 (2013).

Figures

Figure 11: **Experimental setup for cross-grating wavefront microscopy.** (a) Schematic of the microscope. (b) Schematic of the 2D-grating (aka cross-grating) placed at a distance of 0.86 mm from the camera sensor. (c) From left to right, raw camera image called the interferogram, transmittance image, and OPD image, both retrieved from the interferogram.

Figure 12: **IF-DDA numerical simulation of the image of a bacterium**, at focus, on glass in water, modelled as a rod of length 1.5 µm, diameter 0.5 µm and refractive index 1.38 (λ = 550 nm, 1.3NA). (a) Simulated OPD image of the bacterium along with horizontal and vertical crosscuts passing by the center of the bacterium. The dashed line represents the geometry of the bacteria. (b) Estimated optical volume and dry mass as a function of the dilation factor f of the area over which the image integration is numerically performed. The dashed line represents the theoretical values. The dashed lines in the

inset represent the geometries of several integration areas $\mathcal{D}(f)$ for various dilation factors f (1, 2, 4 an 6).

Figure 13: **Procedure of segmentation for dry mass estimation.** (a) Experimental OPD image of a bacterium. (b) Magic-wand selection. (c-e) Segmented areas for various dilation factors f: 0.75, 1 (what the standard segmentation gives) and 1.5 (the minimum segmented area to consider for proper DM estimation). The background value is calcuated over the white, annular area that is 3 px wide. (f) Estimated OV, OP and DM as a function of the dilation factor f.

Figure 14: **Optical volume and dry mass measured on numerical OPD images of 10 micro-objects, simulated using IF-DDA, as a function of the microscope focus.** The morphologies span progressively from a 50-nm sphere to a 4 µm x 2 µm rod. The objects feature a refractive index of $n = 1.38$, are deposited on glass (1.51) and immersed in water ($n_0 = 1.33$). In each case, a drawing of the object is inserted, specifying the dimensions of the object. The dashed lines represent the theorietical OV. The red (darker) lines represent the OV and DM measured on the OPD images by pixel summation, according to Eq. (7) and Eq. (8). The yellow lines represent the weighted OV and DM measured on the OPD images by pixel summation, according to Eq. (13).

Figure 15: **Application of the dry mass estimation algorithm on a noise image.** (a) Simulated OPD noise image (100x100 px). The integration domain $\mathcal{D}$ consists of a disc of radius R. OV and DM estimated using Eqs. (7) and (8) over $\mathcal{D}$ as a function of R. (c) Standard deviation of the measured OV and DM over 5000 noise images, as a function of R, and fit of the profile by the function $R \to aR^2$.

Figure 16 : Optical polarizability, optical volume and dry mass as a function of the integration radius, (a) without any object on the image (only noise), and (b) in the presence of a bacterium.

Figure 17 : **Dependence of dry mass and optica polarisability on focus**. (a) OPD images of a single bacterium for different image focuses (100x, 1.3NA, λ=540 nm). (b) Normalized dry mass as a function of the defocus for 10 different bacteria (dashed lines), along with the average of all these line shapes (solid line). (c) Same as (b) for Re(α). (d) Same as (c) for the Im(α). In (b,c,d), all the line shapes have been normalized by the average value over the range ±2 µm.

Figure 18 : **Dependence of dry mass and optical polarizability on the objective numerical aperture**. (a) OPD images of a single bacterium for different objective numerical apertures (100x, 0.6-1.3NA, λ=540

645 nm). (b) Normalized dry mass as a function of the NA for 10 different bacteria (dashed lines), along with
646 the average of all these line shapes (solid line). (c) Same as (b) for Re(α). (d) Same as (c) for Im(α).
647
648 Figure 19 : **Study of the precision of dry mass measurements.** (a) Optical volume and dry ass
649 measurements for 10 different E. coli bacterial cells, 60 measurements each, represented as box plots.
650 (b) Relative standard deviation of these 10 particular bacteria (100x, 1.3NA, λ=530 nm, exposure time
651 1s).
652
653 Figure 20 : **Examples of microscale colony forming units (mCFU).** (a) mCFU of the Sulfolobus
654 shibatae archaeon. (b) mCFU of the Geobacillus stearothermophilus bacterium. The measured dry
655 masses of the mCFUs are indicated on top of the images. (60x, 1.25NA, λ=625 nm).
656
657 Figure 21 : (a) Dry mass evolution of 5 E. coli mCFUs cultured at 37°C along with the averaged plot. (b)
658 Same data as (a) in a semi-log scale. (c) Dry mass evolution of 2 E. coli mCFUs cultured at 31°c and
659 37°C. 40x air objective, λ=625 nm.
660
661 Figure 22: Complex optical polarizability measurements using CGM for various types of bacteria,
662 namely (a) Escherichia coli, (b) Geobacillus stearothermophilus, (c) Deinococcus radiodurans and (d)
663 Lactobacillus reuteri. (e f, g, h) Examples of OPD images associated with these 4 bacteria species.
664